Mid-infrared signatures of hydroxyl containing water clusters: Infrared laser Stark spectroscopy of OH–H2O and OH(D2O) n (n = 1-3)

Federico J. Hernandez, Joseph T. Brice, Christopher M. Leavitt, Tao Liang, Paul L. Raston, Gustavo A. Pino, and Gary E. Douberly

Citation: The Journal of Chemical Physics **143**, 164304 (2015); doi: 10.1063/1.4933432
View online: http://dx.doi.org/10.1063/1.4933432
View Table of Contents: http://scitation.aip.org/content/aip/journal/jcp/143/16?ver=pdfcov
Published by the AIP Publishing

Mid-infrared signatures of hydroxyl containing water clusters: Infrared laser Stark spectroscopy of OH–H_2O and OH$(D_2O)_n$ (n = 1-3)

Federico J. Hernandez,[1,2] Joseph T. Brice,[1] Christopher M. Leavitt,[1] Tao Liang,[1] Paul L. Raston,[3] Gustavo A. Pino,[2] and Gary E. Douberly[1,a)]

[1]*Department of Chemistry, University of Georgia, Athens, Georgia 30602, USA*
[2]*INFIQC, Dpto. de Fisicoquímica, Facultad de Ciencias Químicas, Centro Láser de Ciencias Moleculares, Universidad Nacional de Córdoba, Ciudad Universitaria, Pabellón, X5000HUA Córdoba, Argentina*
[3]*Department of Chemistry and Biochemistry, James Madison University, Harrisonburg, Virginia 22807, USA*

(Received 10 August 2015; accepted 7 October 2015; published online 23 October 2015)

Small water clusters containing a single hydroxyl radical are synthesized in liquid helium droplets. The OH–H_2O and OH$(D_2O)_n$ clusters (n = 1-3) are probed with infrared laser spectroscopy in the vicinity of the hydroxyl radical OH stretch vibration. Experimental band origins are qualitatively consistent with *ab initio* calculations of the global minimum structures; however, frequency shifts from isolated OH are significantly over-predicted by both B3LYP and MP2 methods. An effective Hamiltonian that accounts for partial quenching of electronic angular momentum is used to analyze Stark spectra of the OH–H_2O and OH–D_2O binary complexes, revealing a 3.70(5) D permanent electric dipole moment. Computations of the dipole moment are in good agreement with experiment when large-amplitude vibrational averaging is taken into account. Polarization spectroscopy is employed to characterize two vibrational bands assigned to OH$(D_2O)_2$, revealing two nearly isoenergetic cyclic isomers that differ in the orientation of the non-hydrogen-bonded deuterium atoms relative to the plane of the three oxygen atoms. The dipole moments for these clusters are determined to be approximately 2.5 and 1.8 D for "up-up" and "up-down" structures, respectively. Hydroxyl stretching bands of larger clusters containing three or more D_2O molecules are observed shifted approximately 300 cm^{-1} to the red of the isolated OH radical. Pressure dependence studies and *ab initio* calculations imply the presence of multiple cyclic isomers of OH$(D_2O)_3$. © *2015 AIP Publishing LLC.* [http://dx.doi.org/10.1063/1.4933432]

I. INTRODUCTION

Hydroxyl containing water clusters are prototype systems for the study of fundamental interactions that underpin chemical processes occurring on the surfaces of atmospheric aerosol particles,[1,2] cloud droplets, and interstellar dust grains.[3–6] Significant progress has been made towards the theoretical characterization of small OH$(H_2O)_n$ clusters.[7–23] Moreover, several recent computational studies have focused on the structural and dynamical properties of OH in bulk aqueous solution,[19,24–26] bulk ices,[27] and on ice surfaces.[27,28] In stark contrast to neutral and ionized water clusters, there remains, however, a dearth of experimental measurements on systems larger than the OH–H_2O binary complex. We present herein a detailed mid-infrared (IR) spectroscopic study of OH$(H_2O)_n$ clusters (n = 1–3), targeting the hydroxyl stretching bands and their evolution with cluster size. The efficient production of these hydroxyl containing water clusters is achieved with a serial doping scheme, in which the individual constituents are loaded into liquid helium droplets and cooled to 0.4 K.

Tropospheric hydroxyl radicals are generated either from the reaction of $O(^1D)$ with H_2O or via the ozonolysis of alkenes, with the latter mechanism dominating during nighttime hours.[29] Recent estimates place the mean global atmospheric concentration of OH during daylight hours on the order of 10^6 molecules cm^{-3}.[29,30] The hydroxyl radical initiates the oxidation of volatile organic compounds (VOCs) within the troposphere.[30–32] OH + VOC hydrogen abstraction reactions produce carbon-centered radicals, which react with $(^3\Sigma^-)O_2$ to produce peroxy radicals that decompose or undergo further bimolecular reactions. Indeed, the processing of tropospheric CH_4 is initiated by its reaction with OH to produce CH_3 and H_2O.[30,32]

Water is the third largest constituent of the troposphere with an average concentration on the order of 10^{17} molecules cm^{-3}, which is sufficiently high to expect a non-negligible abundance of water containing complexes. For example, it has been estimated that the water dimer has an average concentration on the order of 10^{14} molecules cm^{-3}.[20,33] Because of these relatively high concentrations, it has been posited that water vapor affects the rates of atmospheric reactions,[34–36] including those involving the hydroxyl radical.[19,37–41] There is currently significant debate on the role water plays as a catalyst in gas-phase atmospheric reactions.[19,36,41–45] Computational studies have revealed that the presence of a single water molecule lowers energy barriers to product formation in many prevalent tropospheric reactions.[37–41,43] The OH + HO_2 radical termination reaction is an archetypical example; transition state theory predicts the rate constant for O_2/H_2O

a)Author to whom correspondence should be addressed. Electronic mail: douberly@uga.edu. Telephone: 01-706-542-3857.

production to increase by a factor of 10^3 upon addition of a single water molecule (e.g., $OH–H_2O + HO_2$), an effect traced to the formation of doubly hydrogen bonded transition state structures.[41] However, the *effective* rate constant depends parametrically on the gas-phase density of water molecules, and as such, the water catalyzed reaction is too slow to compete with the direct, bimolecular process.[41] This is expected to be a general result, despite the lowering of free energy barriers, and it was indeed also shown to be the case for other prominently discussed water catalyzed reactions.[44] While perhaps not particularly relevant to tropospheric *gas-phase* chemistry, the catalytic properties of water will necessarily play a fundamental role in chemical processes occurring on the surface of aerosol particles, cloud droplets, and other condensed media.[1,2,36] Overview perspectives of the catalytic properties of water and its impact on tropospheric chemistry can be found in Refs. 35 and 36.

As a result of several theoretical and experimental studies,[7,8,21–23,46,47] the structure of the $OH–H_2O$ radical is widely accepted. With *ab initio* computations, two hydrogen-bonded structures were discovered in which the hydroxyl radical acts as either the hydrogen bond donor (**1a**) or acceptor (**1b**).[7,8] Both structures have C_s symmetry, and the **1a** global minimum has two degenerate structures separated by a C_{2v} transition state along the out-of-plane bending coordinate.[8,23] Schaefer and coworkers were the first to find a low lying excited state with $^2A''$ symmetry, which was computed to be ~100 cm^{-1} above the $^2A'$ global minimum.[8] These two electronic states are differentiated by the orientation of the half-filled pπ orbital localized on the hydroxyl radical, which lies either in the symmetry plane ($^2A'$) or perpendicular to it ($^2A''$). Experimental results confirm the global minimum structure predicted *ab initio*,[10,13,14,16,21–23,46,47] with the most convincing characterization coming from the microwave (MW) measurements of Endo and co-workers[16] and Leopold, Marshall, and coworkers.[21,46,47] Francisco and coworkers examined the $OH–H_2O$ global interaction potential and found an A'' to A' state crossing along a path that interconverts isomers **1a** and **1b**, suggesting further investigations into the effect of this low-energy excited state on the reactivity of OH in the presence of water.[17]

There have been several theoretical efforts to elucidate the structures of $OH(H_2O)_n$ clusters and their corresponding effect on the reactivity of the hydroxyl moiety.[15,18–20,24,28,48] Experimentally, to the best of our knowledge, Tsuji and Shibuya have provided the only evidence for any $OH(H_2O)_n$ cluster larger than the binary complex;[22] vacuum ultraviolet (VUV) photoionization of water clusters in solid Ne produces a weak feature in the mid-IR, which they assign to the $OH(H_2O)_2$ trimer.[23] Structurally, hydroxyl containing water clusters adopt either cyclic or cage structures, depending on the number of water molecules in the cluster.[15,18–20] Caged clusters are predicted to be stable minima for clusters as small as $n = 5$ and are globally stable for $n > 5$.

To provide more accurate benchmarks for *ab initio* and molecular dynamics calculations, additional experimental data on $OH(H_2O)_n$ clusters are needed beyond the binary complex. We report herein a first step in this direction via a mid-IR spectroscopic study of these systems in helium droplets. The remainder of the report is organized as follows. Sections II and III describe the experimental and theoretical methods, and Section IV contains the spectroscopic results and analysis. Mass spectra, IR survey spectra, and pressure dependence studies are reported in Sections IV A–IV C, respectively. Rovibrational zero-field and Stark spectra of the $OH–H(D)_2O$ binary complexes are discussed in Section IV D. A vibrational transition moment angle (VTMA) analysis is reported for bands assigned to $OH(D_2O)_2$ clusters in Section IV E, and finally, the spectra of larger clusters are discussed in Section IV F. A summary and outlook for future work is given in Section V.

II. EXPERIMENTAL METHODS

Synthesis of small hydroxyl containing water clusters is achieved via the stepwise doping of individual molecules into nanoscopic droplets of superfluid helium.[49–53] Droplets are formed in a continuous cryogenic nozzle expansion of gaseous helium into vacuum. Nozzle conditions are chosen so as to optimize the production and spectroscopic detection of $OH(D_2O)_2$ clusters. Under these conditions, droplets consisting of ~5000 atoms are produced on average.[49] As the droplets exit the high-pressure region of the nozzle expansion, they cool by evaporation to approximately 0.4 K.[54]

The droplets are skimmed and passed into a differentially pumped vacuum chamber containing an effusive pyrolysis source, from which the OH radical is generated via the thermal decomposition of *tert*-butyl hydrogen peroxide (TBHP), as described elsewhere (Eq. (1)),[55,56]

$$TBHP \xrightarrow{\Delta} \cdot OH + \cdot CH_3 + (CH_3)_2CO. \quad (1)$$

Upon passing through the pyrolysis source, ~12 percent of droplets are doped with a single OH radical, whereas the remaining droplets are either doped with other products of TBHP pyrolysis or are devoid of dopants. The TBHP precursor was purchased from Sigma-Aldrich as a 70% solution in water. Several sequential organic extractions and drying over $MgSO_4$ were carried out to purify the TBHP prior to use. Nevertheless, it was not possible to completely dry the sample, and a small subset of droplets (<1%) are doped with H_2O as they pass through the pyrolysis source. Subsequent to passing through the OH radical source and after ~100 μs of transit time, the droplets pass into a differentially pumped "pick-up cell" (PUC) that contains either H_2O or D_2O vapor at ~10^{-5} Torr. Prior to experiments employing D_2O, the gas lines leading to the PUC were baked overnight and then passivated with D_2O vapor for several hours.

This serial pick-up scheme generates $OH(D_2O)_n$ clusters via the sequential addition of cold monomers. For example, upon pick-up of OH, the translational and internal degrees of freedom of the radical are equilibrated to 0.4 K via He atom evaporation. The timescale associated with this cooling is expected to be fast (< 1 μs) in comparison to the time it takes the droplet to capture an additional molecule (>10 μs).[57,58] The pick-up of a D_2O molecule by an OH doped droplet leads to additional He atom evaporation, as the translational and molecular internal degrees of freedom of D_2O are similarly cooled. The cold OH and D_2O monomers are attracted to each other via

long-range electrostatic interactions, and an OH–D_2O complex is formed in the droplet. Vibrational kinetic energy generated upon hydrogen bond formation is likewise dissipated by He atom evaporation. The timescale for cluster formation upon the addition of a D_2O molecule is significantly less than the time necessary for a subsequent D_2O capture event.[57,58] Therefore, the sequential pick-up of D_2O molecules results in the formation of larger $OH(D_2O)_n$ clusters via the addition of *cold* D_2O monomers to *cold*, pre-formed $OH(D_2O)_{n-1}$ clusters.

After traversing the pick-up zones, the beam of droplets is irradiated with the idler output from a continuous-wave optical parametric oscillator, the tuning and calibration of which has been described elsewhere.[59] Survey spectra are recorded with the laser beam aligned counter-propagating to the droplet beam, whereas the laser is aligned into a two-mirror multipass cell for Stark and polarization spectroscopy measurements, as described elsewhere.[60–62] Vibrational excitation of He-solvated dopants leads to the evaporation of several hundred He atoms, which reduces both the geometric and ionization cross sections of the irradiated droplets. This photo-induced cross section reduction for electron impact ionization is measured with a quadrupole mass spectrometer equipped with a crossed-beam ionizer. The ion-current in either mass channel m/z = 21 u or 19 u (*vide infra* for OH–$(D_2O)_n$ or OH–H_2O, respectively) is pre-amplified and processed with a lock-in amplifier. The laser beam is modulated with a mechanical chopper at 80 Hz and tuned with ~10 MHz resolution. The demodulated ion signal is normalized to laser power, and the frequency axis of each spectrum is established with a high-precision wavemeter, which provides both a relative and absolute frequency calibration.[59]

III. THEORETICAL METHODS

Computations of the geometry, zero-point corrected relative energetics, and vibrational frequencies of several OH $(D_2O)_n$ clusters were carried out with the Gaussian 09 software suite of *ab initio* programs.[63] The computed structures of these clusters are shown in Figure 1, and the results of the computations are summarized in Table I. Although there are a number of previous theoretical reports on $OH(H_2O)_n$ clusters,[7–17,19,21–23] none of these reported dipole moments, vibrational transition moment angles, or anharmonic frequencies. The unrestricted MP2 (uMP2) method was used for the $OH(D_2O)_{1-2}$ calculations, whereas the unrestricted B3LYP (uB3LYP) density functional theory was used for $OH(D_2O)_3$. For both methods, an aug-cc-pVTZ basis set was employed. Calculations of the free hydroxyl radical were used to establish scaling factors for harmonic vibrational frequencies. Anharmonic frequencies are obtained via second-order vibrational perturbation theory (VPT2), as implemented in Gaussian 09. The computations reported here are generally in good agreement with the previous geometry, energy, and harmonic frequency predictions, where comparisons are available.

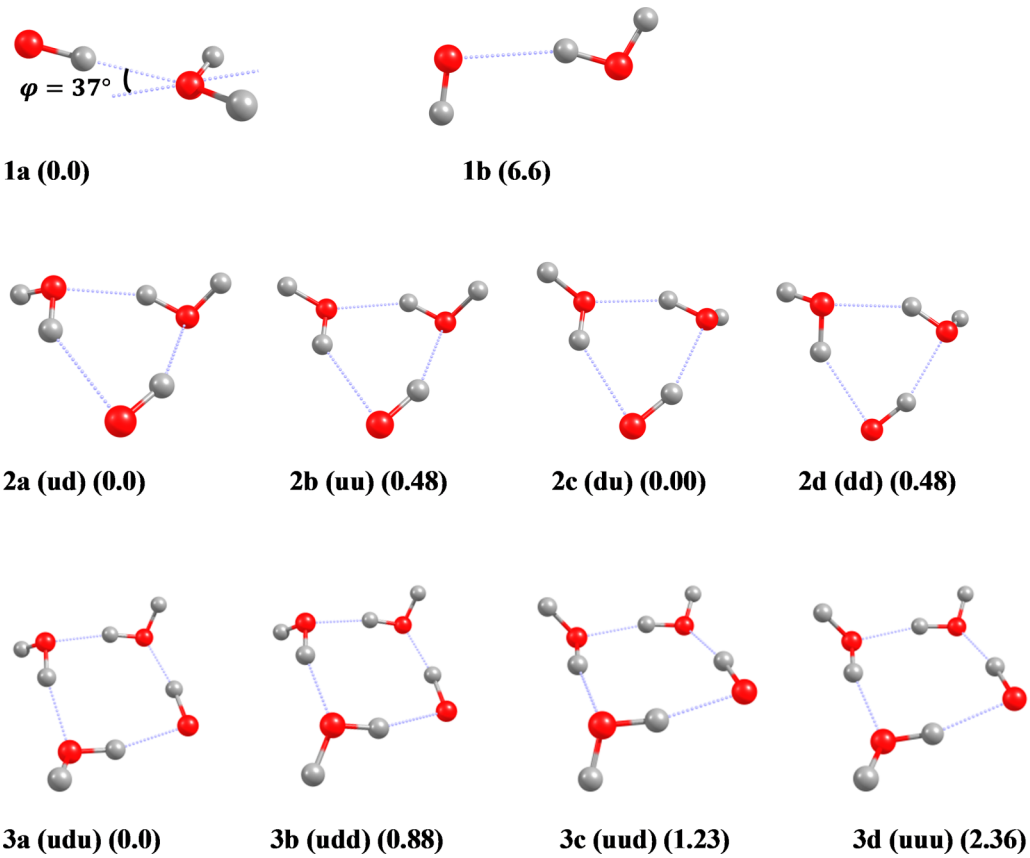

FIG. 1. Optimized geometries of several low energy minima on the $OH(D_2O)_{1-3}$ potential energy surfaces. The **u** or **d** labeling represents the orientation of the non-hydrogen-bonded H atoms of the water molecules (either up or down) relative to the plane of the oxygen atoms. The relative energies (zero-point corrected) for a particular cluster size are given in units of kJ/mol. Energetics of the $OH(D_2O)_{1-2}$ clusters are at the uMP2/aug-cc-pVTZ level, whereas the $OH(D_2O)_3$ energetics are at the uB3LYP/aug-cc-pVTZ level.

TABLE I. *Ab initio* computations of $OH(D_2O)_n$ clusters.

	1a (C_s)	**1a** (C_{2v})[a]	**1b**	
E_{uMP2} (kJ/mol)[b]	0	0.12	6.6	
ω (cm^{-1})[c]	3660 (109)	3676 (307)	3780 (34)	
Δω (cm^{-1})[d]	131	115	11	
ν (cm^{-1})[e]	3445	3460	3558	
Δν (cm^{-1})[f]	123	108	10	
$\|\mu\|$ (D)	4.03	4.20	1.23	
	2a (**ud**)	**2b** (**uu**)	**2c** (**du**)	**2d** (**dd**)
E_{uMP2} (kJ/mol)	0	0.48	0.00	0.48
ω (cm^{-1})[c]	3529 (379)	3534 (378)	3529 (379)	3534 (378)
Δω (cm^{-1})[d]	262	257	262	257
ν (cm^{-1})[e]	3321	3326	3321	3326
Δν (cm^{-1})[f]	247	242	247	242
$\|\mu\|$ (D)	1.76	2.52	1.76	2.52
VTMA (°)	48	63	48	63
	3a (**udu**)	**3b** (**udd**)	**3c** (**uud**)	**3d** (**uuu**)
E_{uB3LYP} (kJ/mol)[g]	0	0.88	1.23	2.36
ω (cm^{-1})[c]	3216 (738)	3218 (749)	3235 (723)	3240 (713)
Δω (cm^{-1})[d]	476	474	457	452
ν (cm^{-1})[e]	3108	3110	3126	3131
Δν (cm^{-1})[f]	460	458	442	437
$\|\mu\|$ (D)	1.66	1.67	1.70	2.78
	OH (**uMP2**)	**OH** (**uB3LYP**)		
ω (cm^{-1})[h]	3791 (20)	3692 (13)		
$\|\mu\|$ (D)[i]	1.67	1.65		

[a]Transition state structure connecting two equivalent C_s minima (**1a**).
[b]Zero-point corrected relative electronic energies (ΔH_0) at the uMP2/aug-cc-pVTZ level. The C_{2v} to C_s comparison for species **1a** is obtained by projecting out the zero-point energy associated with the low-frequency vibrational mode connecting the two equivalent C_s minima.
[c]Harmonic frequency. Intensity in parenthesis (km/mol).
[d]Frequency shift (red) from the computed harmonic frequency of OH.
[e]Scaled harmonic frequency. Scale factor derived from a comparison of OH radical experimental and computed harmonic frequencies (uMP2: 0.9412; uB3LYP: 0.9664).
[f]Frequency shift of scaled harmonic frequency (red) from the experimental OH radical vibrational band origin. For comparison, frequency shifts of experimental bands assigned to $OH(D_2O)_n$ clusters are $n = 1$, 82 cm^{-1}; $n = 2$, 188 and 191 cm^{-1}; $n = 3$, 288, 299, and 335 cm^{-1}.
[g]Zero-point corrected relative electronic energies (ΔH_0) at the uB3LYP/aug-cc-pVTZ level.
[h]For comparison, the experimental band origin is 3568 cm^{-1}.
[i]For comparison, the experimental dipole moment is 1.67 D.

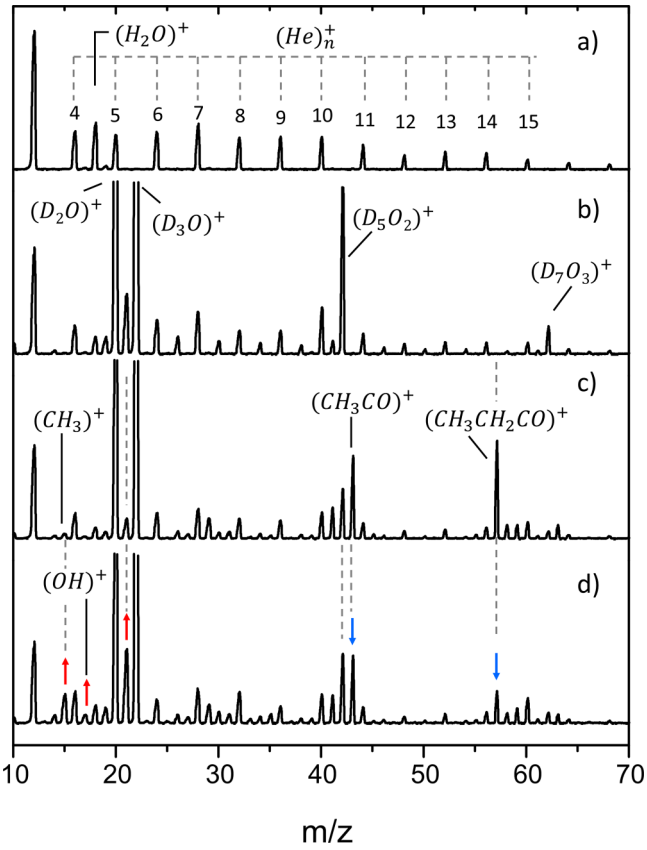

FIG. 2. Mass spectra of (a) the neat droplet beam, (b) the droplet beam doped with D_2O (doping pressure optimized for the pick-up of two D_2O molecules, although a significant fraction of droplets contain other cluster sizes), (c) the droplet beam doped with both D_2O and the pyrolysis precursor TBHP, and (d) the droplet beam doped with both D_2O and the TBHP pyrolysis products (CH_3, acetone, and OH). The blue and red arrows indicate the peaks in the mass spectrum that change qualitatively upon heating the pyrolysis source. The three-fold increase in m/z = 21 upon pyrolysis of TBHP is assigned to the $(HD_2O)^+$ ion that results (at least partially) from the ionization of $OH(D_2O)_n$ clusters.

IV. RESULTS AND DISCUSSION

A. Mass spectrometry

Electron bombardment ionization of He droplets produces helium cluster ions (He_n^+) via mechanism (2), which has been discussed in detail elsewhere,[49,50,64]

$$(He)_n + e^- \rightarrow He^+(He)_{n-1} + 2e^- \rightarrow (He)_2^+(He)_{n-2} + 2e^- \rightarrow (He)_m^+ + (n-m)(He) + 2e^-. \quad (2)$$

Figure 2(a) shows a typical mass spectrum of the neat (undoped) droplet beam, which contains the signature series of mass peaks every 4 u.

Also shown are several mass spectra of the doped droplet beam recorded under various pick-up source conditions (Figs. 2(b)-2(d)). Due to the large energetic mismatch between the ionization potential of He and a molecular dopant (10-15 eV), ionization of the droplet can be followed by the ionization of the dopant via charge transfer from He^+. The energized molecular ion may subsequently undergo fragmentation, which often leads to the appearance of fragment ions similar to those observed in gas-phase electron impact ionization mass spectrometry. Figure 2(b) contains the mass spectrum obtained with D_2O added to the differentially pumped PUC. Ionization of He-solvated D_2O and neat $(D_2O)_n$ clusters proceeds, respectively, according to mechanisms (3a) and (3b), the latter of which is responsible for peaks observed at $2 + (n - q)20$ u, where q runs from 1 to $n - 1$,

$$(D_2O)(He)_m + e^- \rightarrow (D_2O)He^+(He)_{m-1} + 2e^- \rightarrow (D_2O)^{+*} + m(He) + 2e^-, \quad (3a)$$

$$(D_2O)_n(He)_m + e^- \rightarrow (D_2O)_nHe^+(He)_{m-1} + 2e^- \rightarrow (D_2O)_n^+(He)_m + 2e^- \rightarrow D^+(D_2O)_{n-q} + OD^* + (q-1)(D_2O)^* + m(He) + 2e^-. \quad (3b)$$

The outcome of this He^+ charge transfer ionization mechanism (3b) is equivalent to that observed for the electron-impact or

photoionization of gas-phase water clusters, i.e., the production of protonated water clusters.[65,66]

The mass spectrum in Fig. 2(c) was obtained with the simultaneous addition of D_2O vapor to the PUC and TBHP through the effusive, room temperature pyrolysis source. The addition of TBHP to the path of the droplet beam gives rise to peaks in the mass spectrum in the vicinity of 43 u $(CH_3CO)^+$ and 57 u $(CH_3CH_2CO)^+$, which are the known ionization signatures of He-solvated TBHP.[67] The mass spectra in Figs. 2(c) and 2(d) were recorded in sequence, and the only difference in conditions was the temperature of the quartz pyrolysis furnace, either 300 K (Fig. 2(c)) or ~1000 K (Fig. 2(d)). The arrows in the figure indicate the most noticeable changes upon thermal decomposition of TBHP. Most notably, the peak at 21 u depends strongly on pyrolysis conditions and increases with temperature by a factor of 3 to 4. We assign this increase to the appearance of $(HD_2O)^+$ ions produced from droplets containing $OH(D_2O)_n$ clusters. We note, however, that it is not possible to completely eliminate H_2O from either the vacuum system or the TBHP sample, and even under room temperature pyrolysis conditions, a peak at 21 u is observed (Fig. 2(c)), which could arise from the ionization of $H_2O(D_2O)_n$ clusters. Nevertheless, the observed temperature dependence motivated our initial search for the $OH(D_2O)_n$ spectrum as laser-induced ion signal modulation on channel 21 u. The depletion spectrum recorded in this channel is expected to be largely free from bands associated with other species present in the droplet ensemble. For example, the He^+ charge transfer ionization of He-solvated $(CH_3)_2CO$–D_2O is expected to produce $(CH_3)_2COD^+$, because the proton affinity difference between acetone and water is ~126 kJ/mol.[68] Indeed, as evident in Figs. 2(c) and 2(d), m/z = 60 u increases upon heating the pyrolysis furnace.

B. Survey spectra

The laser-induced depletion spectrum in Fig. 3 was obtained under conditions equivalent to those used to record the mass spectrum in Fig. 2(d). The PUC pressure was optimized for the production of clusters containing two D_2O molecules, although we note that the statistical pick-up process necessarily leads to a distribution of cluster sizes in the droplet ensemble.[49,50,69] The spectrum covers the hydrogen-bonded OH stretching region of neutral water clusters, and the band origin of free OH is 3568.4 cm^{-1}.[56] As expected, the m/z = 21 u channel discriminates against the spectra of H_2O containing clusters that may arise from the pick-up of residual H_2O molecules in the vacuum system; for example, an intense band at 3597 cm^{-1} due to $(H_2O)_2$ is completely absent. Replacing H_2O with D_2O in these measurements also red shifts the hydrogen-bonded stretching vibrations localized on water moieties within hydroxyl-water clusters, thereby revealing the hydroxyl stretching band associated with each cluster.

An intense band at 3485.6 cm^{-1} is close in frequency to the hydroxyl stretch band of the OH–H_2O complex observed in the gas-phase (3491.3 cm^{-1})[23] and in Ne matrixes (3472.5 cm^{-1}).[22] The rotational substructure associated with this band (*vide infra*) confirms its assignment to OH–D_2O. The large red shift from free OH (82 cm^{-1}) is characteristic of the hydrogen bonded geometry, in which the hydroxyl radical acts as

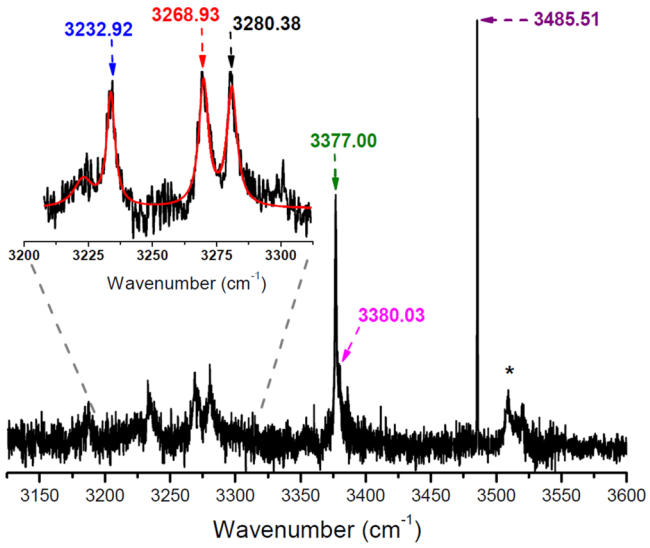

FIG. 3. Survey scan of $OH(D_2O)_n$ clusters in the OH stretching region (m/z = 21 u depletion). The sharpest band at 3485.51 cm^{-1} is assigned to the OH stretch of the binary OH–D_2O complex, and the two bands at 3377 and 3380 cm^{-1} are assigned to two separate isomers of the cyclic $OH(D_2O)_2$ trimer. The weak features between 3150 and 3300 cm^{-1} are assigned to clusters containing at least three D_2O molecules. The inset is the average of multiple scans in this frequency region, and the red line is a simulation of four Lorentzians fitted to the data. The asterisk marks a band that does not depend on pyrolysis source temperature.

hydrogen donor, binding to H_2O in an approximately C_{2v} configuration (**1a**). Another isomer (**1b**) is predicted on the OH–H_2O potential energy surface 6.8 kJ/mol above the global minimum. Isomer **1b** is planar with OH acting as the hydrogen bond acceptor. In this configuration, calculations predict the stretching vibration localized on the hydroxyl moiety to be shifted 11 cm^{-1} to the red of isolated OH, and there is no evidence for this species in the survey spectrum.

Computations reveal cyclic clusters as global minima for $n > 1$, in which OH resides within the ring and acts as both hydrogen donor and acceptor (**2a**-**3d**). Analogous to small neutral water clusters, we expect hydrogen bond cooperativity effects in these cyclic clusters to red shift the hydroxyl vibration well beyond that observed for OH–D_2O. Indeed, *ab initio* calculations presented here and elsewhere predict successively larger OH stretching red shifts with increasing cluster size (Table I).[15,19,22] A broader feature at 3377 cm^{-1} is in the same vicinity as a weak feature observed upon VUV photolysis of $(H_2O)_n$ clusters in solid-Ne (3365 cm^{-1}), which Tsuji and Shibuya assigned to $OH(H_2O)_2$.[22] Assuming a preliminary assignment of the 3377 cm^{-1} band to $OH(D_2O)_2$, the addition of the second D_2O and formation of the ring results in an additional 109 cm^{-1} red shift of the hydroxyl stretch. A somewhat weaker feature centered at 3380 cm^{-1} is situated as an unresolved shoulder to the blue of the intense band.

Even broader bands are observed in the 3150–3300 cm^{-1} region, each having an approximately 5 cm^{-1} line width. An average of several scans in this region is shown in the inset, and a fit to four Lorentzians is shown in red, which approximately establishes the band origins of these features. On the basis of frequency shift alone, it is reasonable to assign these features

to stretching bands of $OH(D_2O)_n$ clusters with $n > 2$, in which the vibrational amplitude is largely localized as OH stretching.

As noted above, it is difficult to completely eliminate H_2O from the vacuum system and TBHP sample, and OH stretching bands associated with $H_2O(D_2O)_n$ clusters are also expected to fall in this frequency region and perhaps produce depletion in mass channel 21 u. Therefore, we carefully verified that the bands labeled in Fig. 3 disappeared upon cooling the pyrolysis furnace to room temperature. The feature marked with an asterisk, however, remained at all pyrolysis conditions.

C. Pressure dependence

The peak intensity of each band labeled in Fig. 3 was measured as a function of D_2O pressure in the PUC. The PUC pressure curves shown in Fig. 4 are consistent with the aforementioned cluster size assignments. The curves in Fig. 4 are color coded to match the labels in Fig. 3, and it is evident that the bands at 3377.0 and 3380.0 cm^{-1} are optimized at approximately twice the pressure required to optimize the band at 3485.6 cm^{-1}. Together with the observed frequency shifts, this characteristic D_2O pressure dependence supports an assignment of the 3377.0/3380.0 and 3485.6 cm^{-1} bands to $OH(D_2O)_2$ and OH–D_2O clusters, respectively.

Because of the rather weak signal associated with the bands in the 3150–3300 cm^{-1} region, the PUC curves for these features are less definitive, although they each qualitatively appear to peak at higher pressures than observed for the two $OH(D_2O)_2$ bands, consistent with an assignment to $OH(D_2O)_3$ or larger clusters.

D. OH–H(D)$_2$O

Ab initio calculations of the OH–H_2O potential surface predict an A' equilibrium geometry (**1a**), in which the singly occupied pπ orbital is aligned within the symmetry plane.[8] An electronic state of A'' symmetry is predicted to be 100–200 cm^{-1} higher in energy.[8,9,12,70] The minimum energy **1a** structure has an out-of-plane angle, $\varphi = \pm 37°$, which is defined as the angle between the intermolecular O–O axis and the HOH bisector (Fig. 1(a)).[23] A C_{2v} transition state structure ($\varphi = 0°$) connects the two equivalent C_s minima. The electronic symmetry of this transition state is B_1, with the pπ orbital pointing out of the molecular plane. The barrier to planarity on the A' out-of-plane bending potential has been computed by McCoy, Lester, and co-workers to be 24.3 cm^{-1} at the B3LYP/aug-cc-pVTZ level.[23] The zero-point level in this potential is ~15 cm^{-1} above the interconversion barrier,[23] and the geometry of this system has been described as being "effectively" C_{2v}.[21,46]

Microwave spectroscopy of gas-phase OH–H_2O confirms via hyperfine splitting that the $^2A'$ electronic state is the global minimum.[21,46,47] Partial quenching of orbital angular momentum upon complex formation leads to parity doubling of rotational levels,[71,72] the extent of which reveals the energetic separation between $^2A'$ and $^2A''$ states.[21,46,47] In the absence of spin-orbit coupling, the $^2A''$ state is located 146.56 cm^{-1} above the $^2A'$ ground state. Accounting for spin-orbit coupling, the two states are split by 203.76 cm^{-1}.[21,46]

Figure 5 shows higher-resolution scans of the hydroxyl stretching bands of both OH–H_2O and OH–D_2O. A model for the rotational structure that accounts for partial quenching of electronic angular momentum[71–73] was used to generate the simulations shown as red traces in the figure. The physical constants used to generate the simulations are summarized in Table II. The two spectra (H_2O vs. D_2O) differ qualitatively,

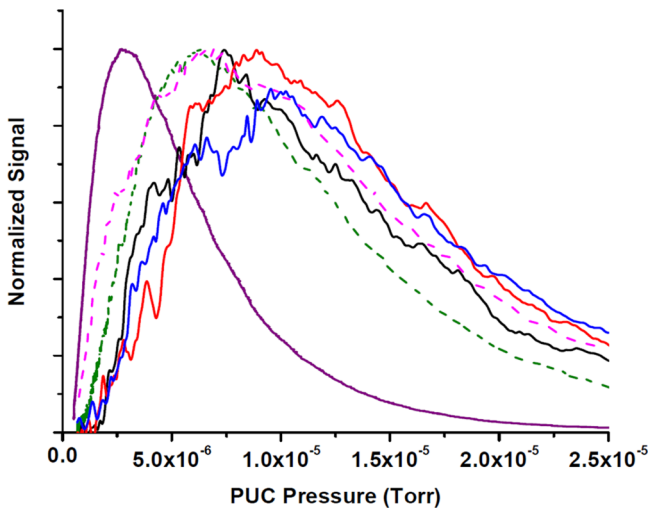

FIG. 4. Pick-up cell pressure curves (D_2O pressure) for the OH stretch bands labeled in Fig. 3. The color of each curve indicates the frequency of the IR laser, which is given in Fig. 3. The pressure corresponds to the uncorrected output from an ion gauge attached to the differentially pumped pick-up cell.

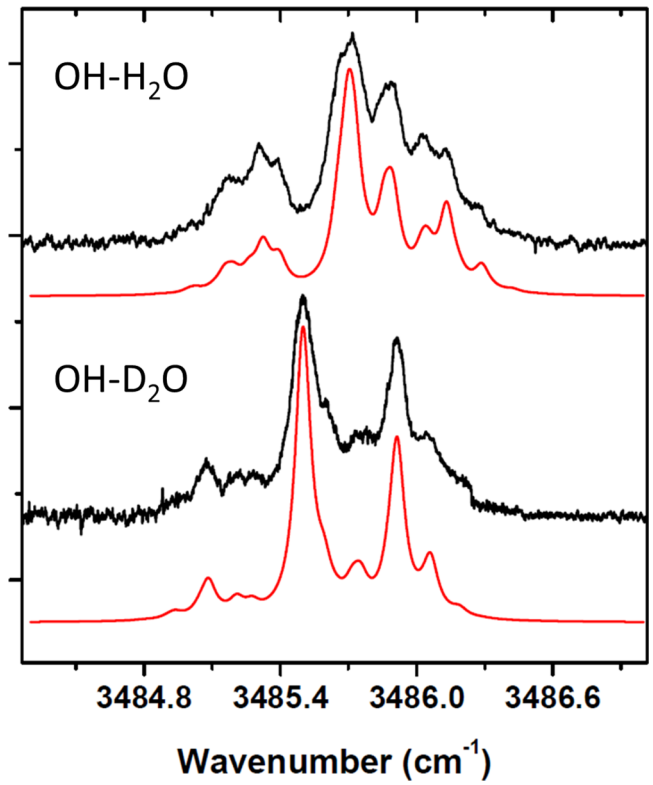

FIG. 5. Zero-field higher-resolution scans of the OH stretch bands associated with OH–H_2O and OH–D_2O binary complexes. The red traces are simulations based on a model for the rotational energy levels that accounts for partially quenched electronic angular momentum.[71–73] The qualitative difference between the two bands derives from the different nuclear spin statistical weights associated with the equivalent H and D atoms of the water moiety.

TABLE II. Spectroscopic parameters (in cm^{-1}) determined from simulations of the a-type spectra of OH–H_2O and OH–D_2O.[a]

	Helium (OH–H_2O)	Helium (OH–D_2O)	Gas (OH–H_2O)
ν_0	3485.815 (1)	3485.600 (1)	3490[b]
μ'' (D)	3.70 (5)	3.70 (5)	
μ' (D)	3.75 (5)	3.75 (5)	
A''	13.4	6.4	
ΔA[c]	−0.29	−0.20	
$(B+C)/2$[d]	0.090	0.086	0.2195[e]
D_J[d]	0.000 46	0.000 46	
ρ[d]	−146 (5)	−146 (5)	−146.56[e]
Γ	0.08	0.08	
T_{rot} (K)	0.35	0.35	

[a]Numbers in parentheses are 2σ uncertainties in the last digit. The spin-orbit coupling constant was fixed at −139.0508 cm^{-1} in the simulations. The constant $(B-C)/2$ is constrained to be equal to zero. The gas-phase value of this constant, determined from MW spectra, is 50 MHz.[46] Moreover, the a-type spectra are insensitive to A'', which is constrained to its *ab initio* value.
[b]From Ref. 23.
[c]The change is taken as the excited state minus the ground state constant.
[d]The ground and excited state constants are the same.
[e]From Ref. 46.

because of the different nuclear spin statistical weights associated with the interchange of either identical H or D atoms. Nevertheless, a similar set of constants produce satisfactory simulations for both experimental spectra.

The $(B + C)/2$ rotational constant for He-solvated OH–H_2O is reduced from the gas-phase value by a factor of 2.4, which is consistent with the expected increase in moment of inertia for rotation within the liquid.[50] Although simulations of these a-type rovibrational bands are insensitive to the value of the A rotational constant, they are quite sensitive to changes in the A constant upon vibrational excitation. An approximately 0.2–0.3 cm^{-1} decrease in the A constant upon hydroxyl stretch excitation is observed for both isotopologues. This is consistent with the calculations of McCoy, Lester, and coworkers,[23] which predict both an increase in interconversion barrier height (+30 cm^{-1}) and equilibrium bend angle (+5°) upon vibrational excitation. Both of these effects increase the vibrationally averaged bending angle, leading to a reduction in the A rotational constant. For example, the A constant is reduced by 0.8 cm^{-1} in going from the C_{2v} structure to the C_s equilibrium geometry at the uMP2 level.

The rotational substructure also allows for an analysis of the $^2A'$–$^2A''$ energetic separation, which is referred to as the "difference potential" and given the label ρ.[71,72] As discussed elsewhere,[71,72] the rotational energy level pattern is qualitatively sensitive to this energy difference. Despite the relatively broad line widths (0.08 cm^{-1}) that wash out much of the substructure, the simulations reveal this energy difference to be −146(5) cm^{-1} for the He-solvated complex, where the uncertainty is derived from the sensitivity of the rotational contours to changes in the ρ fitting parameter. Within this relatively large uncertainty, the value extracted from the He droplet spectrum is in agreement with the gas-phase value.[21,46] In a previous report on the spectroscopy of OH–C_2H_2,[73] we found that the helium solvent made ρ more negative by 13 cm^{-1}, and we suggested a difference in free energies of solvation for the two electronic states as the origin of this effect. The effect of the solvent on ρ will depend sensitively on the molecule-He interaction potential. Apparently, the helium solvation energy of the OH–H_2O radical is less sensitive to the orientation of the singly occupied pπ orbital, in comparison to OH–C_2H_2.

We recently reported an effective Hamiltonian approach for modeling the Stark effect in polyatomic open shell complexes that exhibit partially quenched electronic angular momentum.[74] With this model, we can extract permanent electric dipole moments from Stark spectra of the OH–H(D)$_2$O complexes. Figures 6 and 7 show Stark spectra for OH–D_2O and OH–H_2O, respectively. Spectra were recorded at multiple electric field strengths and with laser polarization alignments either parallel or perpendicular to the Stark field. Simulations of the Stark effect were carried out with rotational constants determined from the zero-field spectra. For both isotopologues, simulations closely reproduce the experimental spectra when ground and excited vibrational state dipole moments are set equal to 3.70 and 3.75 D, respectively. The uncertainty is estimated to be ± 0.05 D, and within this uncertainty, the dipole moment does not exhibit an isotopic dependence. For comparison, the uMP2 dipole moment at the C_{2v} geometry is 4.20 D, whereas it is 4.03 D at the C_s minimum. However, the experiment necessarily probes the expectation value of the dipole component along the a-inertial axis, which corresponds to the OH–O axis for the C_{2v} structure. By symmetry, the b-axis component is zero and the c-axis component changes sign as the complex interconverts between equivalent C_s minima along the out-of-plane bend coordinate. As the complex bends from planarity, the a-axis dipole component varies from 4.20 D at $\varphi = 0°$ to 3.47 D at $\varphi = \pm 55°$. Using the numerical approach described by McCoy, Lester, and co-workers,[23] we find that the expectation value of μ_a along the one-dimensional bend potential is 3.87 D, which is in reasonable agreement with experiment.

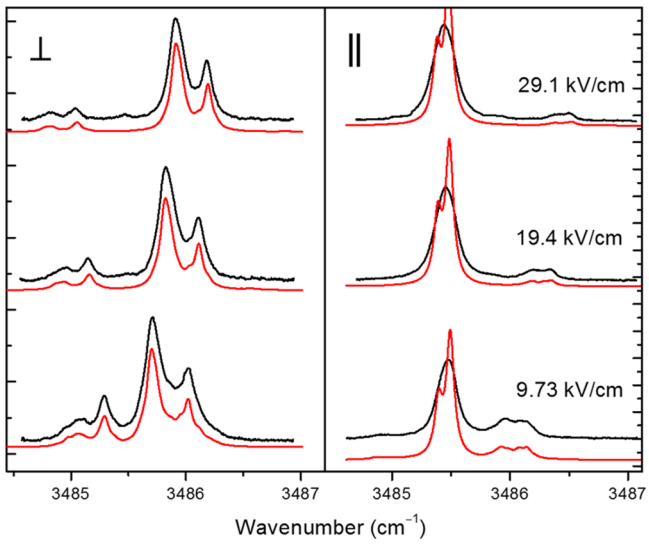

FIG. 6. Stark spectra of the OH stretch band of the binary OH–D_2O complex. The field strengths and laser polarization configurations, relative to the static Stark field, are shown along the right and top of the figure, respectively. The red traces are simulations based on a model that accounts for partial quenching of electronic angular momentum,[74] and the ground and excited vibrational state dipole moments extracted from the simulations are 3.70(5) and 3.75(5) D, respectively.

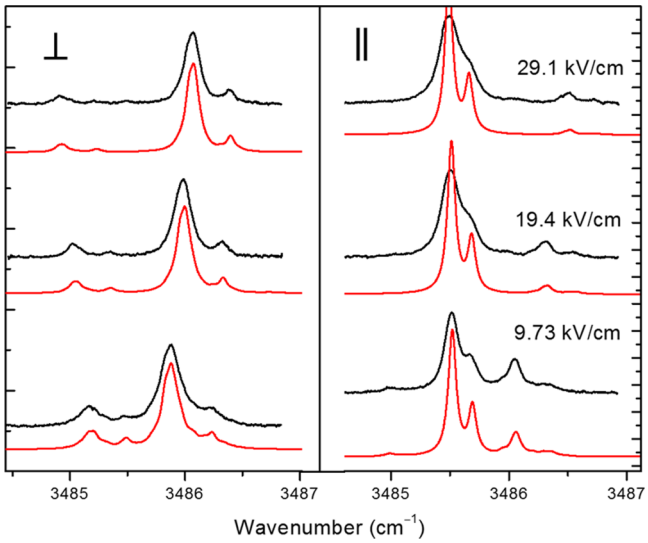

FIG. 7. Stark spectra of the OH stretch band of the binary OH–H_2O complex. The field strengths and laser polarization configurations, relative to the static Stark field, are shown along the right and top of the figure, respectively. The red traces are simulations based on a model that accounts for partial quenching of electronic angular momentum,[74] and the ground and excited vibrational state dipole moments extracted from the simulations are 3.70(5) and 3.75(5) D, respectively.

The hydroxyl stretching band of the OH–H_2O complex has been observed in solid Ar (3452.2 cm^{-1}),[13,14] solid Ne (3472.5 cm^{-1}),[22] and in the gas-phase (3491.3 cm^{-1}).[23] The band origin in He droplets (3485.8 cm^{-1}) is shifted from the gas-phase value by −5.8 cm^{-1}. Although this would normally be viewed as a rather large droplet-induced frequency shift, similar effects have been observed for other strongly hydrogen bonded binary complexes in He droplets. For example, the high frequency X–H stretching bands in HCN–HF exhibit qualitatively different solvent shifts. The "free" CH stretch exhibits a rather typical 0.4 cm^{-1} shift to the red, whereas the hydrogen bonded HF stretch is shifted by -11.9 cm^{-1}.[53] Collecting the solvent shifts for several similarly hydrogen bonded binary systems,[50] an approximately linear relationship between solvent shift and complexation-induced frequency shift was revealed. Employing this linear relationship (see Fig. 21 of Ref. 50), the solvent shift for the hydroxyl stretch in the OH–H_2O complex is predicted to be −5 cm^{-1}. The origin of this relationship has yet to be established theoretically, but it has been posited that the effect may be at least partially due to a solvent-induced reduction of low frequency bending amplitudes.[53] This effective stiffening of the complex can, in principle, enhance the hydrogen bonding interaction. For example, a stiffer bending potential results in a vibrationally averaged HCN–HF structure closer to linearity, where the complexation-induced frequency shift of the HF stretch is maximized.[53] Considering the computed harmonic frequencies for the **1a** structures, we find that the hydroxyl stretch frequency increases by 16 cm^{-1} in going from the minimum energy structure (C_s) to the transition state (C_{2v}) along the large amplitude bending potential, an effect which has been discussed by McCoy, Lester and co-workers.[23] If the He solvent were to increase the effective barrier height along this bending potential, then the vibrationally averaged structure would become less "C_{2v} like," resulting in an enhanced complexation-induced frequency shift, as observed experimentally. A similar effect is expected if the solvent were to add to the reduced mass for motion along the bending potential. It is interesting to note that these stiffening effects would also act to reduce the expectation value of the *a*-axis dipole moment component. Perhaps this can explain the residual discrepancy between the experimental ($\langle\mu_a\rangle$ = 3.70(5) D) and *ab initio* vibrationally averaged ($\langle\mu_a\rangle$ = 3.87 D) results.

The higher energy local minimum, **1b**, is conspicuously absent in all experimental studies to date. We searched carefully for this species, as He droplets have been shown to facilitate the formation of higher energy cluster species via rapid cooling of the condensing molecular system.[50,52,53,57,75] For example, in addition to the linear HCN–HF isomer, sequential pick-up of HCN and HF results in the formation of a higher energy HF–HCN bent isomer.[53] The HF–HCN structure is observed despite it being 20 kJ/mol higher in energy than HCN–HF. A 6.4 kJ/mol barrier, submerged 5.0 kJ/mol below the asymptote, separates the bent isomer from the linear global minimum.[53]

To gain further insight into the outcome of OH–H_2O cluster formation, a potential energy scan at the uMP2/aug-cc-pVTZ level of theory was carried out to locate the barrier between isomers **1a** and **1b**. Starting from structure **1b** ($^2A''$), the hydroxyl moiety was rotated towards **1a** ($^2B_1$), while constraining the system to be planar and allowing all other degrees of freedom to relax. This scan finds a meager 0.7 kJ/mol barrier separating **1b** from **1a**. The exact barrier height at this level of theory will necessarily be smaller, because the distinguished reaction path employed here is an approximate representation of the minimum energy pathway for interconversion. It should be emphasized that the interconversion barrier is submerged 12.8 kJ/mol below the OH + H_2O energetic asymptote. A 0.7 kJ/mol barrier may simply be insufficient to prevent the rearrangement of **1b** on the timescale for cooling. Another consideration is the effect long-range interactions have in steering the system on the potential surface as the fragments approach within the droplet. For example, the most energetically favorable long range approach trajectory corresponds to a fragment configuration in which the two dipole moments are aligned. Clearly, this arrangement favors the production of **1a**, which has a dipole moment ~3 D larger than **1b**.

E. OH(D_2O)$_2$

The bottom frame in Fig. 8 is a higher-resolution zero-field scan in the vicinity of the 3377 and 3380 cm^{-1} bands labeled in Fig. 3. As discussed above, these bands are assigned to OH(D_2O)$_2$ on the basis of frequency shift from OH monomer and PUC pressure dependence curves (Fig. 4). Both bands are satisfactory reproduced by fitting the data to two separate Lorentzian line shape functions (Fig. 8; red trace in bottom frame). The 3377 and 3380 cm^{-1} bands have 1.3 and 3.2 cm^{-1} full-width at half-maximum line widths, respectively. These widths are similar to those previously observed for hydrogen bonded OH stretching bands of cyclic (H_2O)$_3$ clusters in He droplets.[52] We posit that these two bands are due to separate isomers of OH(D_2O)$_2$. Calculations find two stable

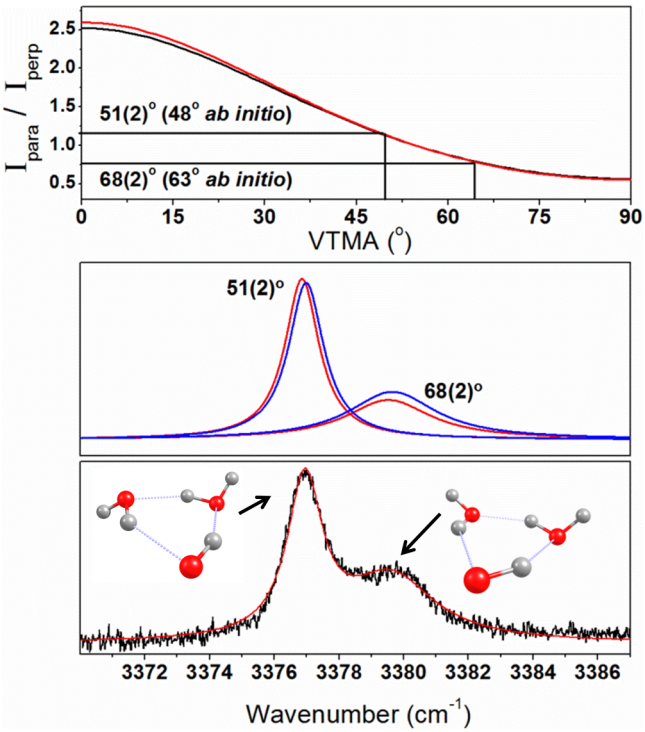

FIG. 8. Vibrational transition moment angle analysis of the bands assigned to cyclic isomers of $OH(D_2O)_2$. The bottom frame is a higher-resolution zero-field scan in the vicinity of the 3377 and 3380 cm^{-1} bands in Fig. 3. The structures of the two cyclic trimers and the associated assignments are shown as insets. The middle frame contains the Lorentzians obtained from fitting the high-field spectra (31.0 kV/cm) obtained with parallel (red) and perpendicular (blue) polarization configurations. The Lorentzian areas are normalized to zero-field values obtained with an identical fitting procedure. The top frame shows the computed parallel to perpendicular intensity ratios expected at high-field versus VTMA for the **ud**/**du** (black) and **uu**/**dd** (red) cyclic trimers. Using the computed intensity ratio curve, the experimental intensity ratios are used to obtain semi-empirical VTMAs of 51(2)° and 68(2)° for the 3377 and 3380 cm^{-1} bands, respectively. These values compare favorably to the *ab initio* VTMAs computed for the OH stretch bands of the **ud**/**du** (48°) and **uu**/**dd** (68°) cyclic trimers.

cyclic minima that differ in the orientation of the non-hydrogen bonded D atoms relative to the plane of the oxygen atoms (either *up* or *down*) (Fig. 1). We label these **2a** (**ud**) and **2b** (**uu**) for "up-down" and "up-up" isomers, respectively. The isomer having both D atoms pointing "up" is 0.48 kJ/mol higher in energy than the **ud** isomer at the zero-point corrected uMP2/aug-cc-pVTZ level. At this level of theory, harmonic frequency calculations predict the hydroxyl stretch bands to be split by 5 cm^{-1}, which is consistent with experiment. We also carried out VPT2 anharmonic frequency calculations for these two isomers, and the predicted separation between the hydroxyl stretch bands is reduced to ~1 cm^{-1}. Two other isomers are found that differ only in the phase of the hydrogen bonds (Fig. 1). The **2c** (**du**) and **2d** (**dd**) isomers are isoenergetic to **2a** and **2b**, respectively, and frequency calculations return equivalent results for each isoenergetic pair (Table I).

Unlike the spectra of $OH–H(D)_2O$, where rotational fine structure allowed us to make a definitive assignment, the $OH(D_2O)_2$ bands are broadened beyond the rotational contour, likely due to a homogeneous mechanism involving rapid vibrational deactivation. Nevertheless, polarization spectroscopy can be used to support the assignments. Polarization spectroscopy involves the laboratory frame orientation of polar molecules using a relatively large static electric field (31.0 kV/cm). Vibrational band intensities are measured with laser polarization alignments either parallel or perpendicular to the orienting field.[60] As discussed in detail elsewhere, the parallel to perpendicular intensity ratio for a given field strength will depend sensitively on the angle between the vibrational transition moment and the permanent dipole moment of the molecule.[60,61,76–78] If the VTMA is <54.75°, the intensity ratio will be >1, whereas if the angle is >54.75°, the ratio will be <1.

The middle frame in Fig. 8 shows Lorentzian line shape functions that were fitted to the spectra measured under high-field conditions. The red and blue curves correspond to fits of spectra measured with parallel and perpendicular laser polarizations, respectively. The intensity changes are small for both bands, indicating VTMAs close to the 54.75° magic angle. Nevertheless, the changes are informative, as the intensity dependence on laser polarization is qualitatively different. The lower frequency band *increases* in intensity with parallel polarization, whereas the higher frequency band *decreases* in intensity; the opposite is observed for perpendicular polarization measurements. In determining the parallel to perpendicular intensity ratio at high-field, each spectrum was fitted to two Lorentzians, and the areas obtained from this fitting procedure were normalized to the corresponding zero-field values recorded under identical polarization conditions. The I_{para} : I_{perp} ratios are 1.1 and 0.72 for the 3377 and 3380 cm^{-1} bands, respectively.

The top frame in Fig. 8 shows the computed parallel to perpendicular intensity ratios expected for a 31 kV/cm orienting field as a function of VTMA for the **ud**/**du** (black) and **uu**/**dd** (red) cyclic trimers. Using the computed curve,[50,60] the experimental intensity ratios are used to obtain semi-empirical VTMAs of 51(2)° and 68(2)° for the 3377 and 3380 cm^{-1} bands, respectively. These VTMAs are necessarily semi-empirical, because the "calibration" curves are computed with *ab initio* permanent dipole moments as input. These semi-empirical values compare favorably to the *ab initio* VTMAs computed for the OH stretch bands of **ud**/**du** (48°) and **uu**/**dd** (68°) cyclic trimers. The polarization spectroscopic analysis presented here is consistent with an assignment of the 3377 and 3380 cm^{-1} bands to the hydroxyl stretch vibrations within the **2a**/**c** (**ud**/**du**) and **2b**/**d** (**uu**/**dd**) structures, respectively. Unlike for the formation of the binary complex, it is not obvious that long range interactions between a preformed $OH–D_2O$ and an approaching D_2O molecule should bias the population of trimer isomers. Indeed, the integrated areas of the two bands are the same within the error of the experiment.

The above assignment is satisfying, as it is based on frequency computations, PUC curves, and VTMA analysis. However, it is reasonable to question the feasibility for stabilizing the higher energy **2b**/**d** (**uu**/**dd**) isomers in He droplets. The **2a**/**c** and **2b**/**d** $OH(H_2O)_2$ clusters are geometrically related to the cyclic water trimer; that is, with one of the non-bonded H atoms removed. On the water trimer potential surface, in the vicinity of the cyclic structure, there are 96 equivalent minima connected by various tunneling pathways, such as "flipping" of the non-bonded H atoms from one side of the plane to another

via a C_{3h} transition state.[79] The barrier associated with this flipping motion has been computed to be ~0.5 kJ/mol.[80] Removing one non-bonded H atom reduces the symmetry of the system from G_{96} to C_1, but a similar pathway can nevertheless be imagined that interconverts **2b** to **2a** over a relatively low barrier. A relaxed potential scan (uMP2/aug-cc-pVTZ) finds a 1.9 kJ/mol interconversion barrier along the **2b** to **2a** pathway corresponding to the "up" to "down" flipping of one non-bonded H atom. Perhaps it is not unreasonable that a barrier of this magnitude could result in the kinetic trapping of **2b**/**d** (**uu**/**dd**) as cluster condensation energy is dissipated by He atom evaporation; indeed, this would not be an unprecedented observation, as non-equilibrium $(HF)_5$ clusters were observed to be stabilized behind barriers of similar magnitude upon formation in He droplets.[75]

F. $OH(D_2O)_{n>2}$

Broad features in the 3150–3300 cm^{-1} range have PUC pressure dependences that suggest an assignment to larger clusters with $n > 2$. Although these bands are clearly absent with the pyrolysis furnace cooled to room temperature, the signals are too weak to perform the polarization spectroscopy analysis discussed above. There are several factors contributing to the signal being weak in this frequency region, despite the prediction of large IR oscillator strengths; for example, He^+ charge transfer ionization of $OH(D_2O)_{n>2}$ clusters is expected to produce a distribution of $H^+(D_2O)_n$ ions, thereby diluting the laser-induced depletion signal. Furthermore, the probability for forming $OH(D_2O)_n$ clusters via sequential pick-up decreases rapidly with increasing n; for example, we estimate that optimized conditions produce $OH(D_2O)_3$ as only 2 percent of the droplet ensemble. Finally, *ab initio* computations (Fig. 1 and Table I) find several nearly isoenergetic isomers of $OH(D_2O)_3$, each with distinctly different OH stretching band origins.

In analogy to $OH(D_2O)_2$, four cyclic $OH(D_2O)_3$ isomers are optimized, which differ only in the orientation of the non-bonded D atoms relative to the plane of the oxygen atoms. The formation of cyclic clusters is likely upon addition of the third D_2O molecule. Indeed, for $(H_2O)_n$ clusters, ring insertion into the trimer to form a cyclic tetramer is barrierless on the zero Kelvin enthalpic potential surface.[81] The lowest energy $OH(D_2O)_3$ isomer has an alternating "up-down-up" configuration, whereas the highest energy isomer (+2.36 kJ/mol) has an "up-up-up" configuration. The orientation of the non-bonded D atoms has a relatively large impact on the hydroxyl stretching band. The **3a** (**udu**) and **3b** (**udd**) isomers are predicted to have bands separated by only ~2 cm^{-1}; but in going to the **3c** (**uud**) and **3d** (**uuu**) isomers, an additional red shift of ~20 cm^{-1} is predicted. An assignment of bands in the He droplet spectrum to any of these species would be speculative, although the presence of multiple bands in this region suggests the stabilization of multiple isomers. We note that calculations systematically over predict the frequency shifts of $OH(D_2O)_n$ hydroxyl stretching bands from the OH monomer origin (3568 cm^{-1}). For the n = 1, 2, and 3 clusters, frequency shifts at the uMP2/aug-cc-pVTZ level are 120, 240, and 437–460 cm^{-1}, respectively, as shown in Table I. Experimental shifts are 82, 191, and 288–335 cm^{-1}, in comparison. Survey spectra were measured as far down as 450 cm^{-1} to the red of the hydroxyl radical stretch band, yet no other bands were observed below the set of features considered here. It would be interesting in future studies to explore more efficient sources of the hydroxyl radical, for example, photolysis of H_2O_2. Combined with multiplexed detection of $H^+(D_2O)_n$ ions via time of flight mass spectrometry, these improvements may allow for a more detailed characterization of the larger cluster species discovered in this work.

V. SUMMARY

Water clusters containing the hydroxyl radical were formed in He droplets via a serial pick-up scheme and probed with IR laser spectroscopy. OH–H_2O and $OH(D_2O)_n$ clusters up to $n = 3$ were observed in the frequency range 3125–3600 cm^{-1}.

Partially resolved rotational substructure is observed for the hydroxyl stretching bands of OH–H_2O and OH–D_2O binary complexes centered near 3486 cm^{-1}. An analysis of this fine structure reveals the extent to which the He solvent modifies the gas-phase molecular constants. Within the experimental uncertainty, the He solvent does not modify orbital angular momentum quenching in the complex, and the energy difference between $^2A'$ and $^2A''$ electronic states is the same as in the gas phase (~146 ± 5 cm^{-1}). Stark spectroscopy provides the permanent electric dipole moment for each complex. Specifically, Stark spectroscopy probes the expectation value of the dipole component along the a-inertial axis of each binary system, which corresponds approximately to the OH–O axis. For both isotopologues, the ground vibrational state dipole moment is $\langle \mu_a \rangle$ = 3.70(5) D. In comparison, a vibrationally averaged $\langle \mu_a \rangle$ equal to 3.87 D is obtained by averaging over the one-dimensional bending potential that interconverts equivalent C_s minima via a C_{2v} transition state. A relatively large 5.8 cm^{-1} solvent shift is observed for the hydroxyl stretching bands of these complexes. Both the red shift and the reduced dipole moment are consistent with a solvent induced stiffening of the complex with respect to the out-of-plane bending coordinate, making the complex more bent on average.

In combination with quasi-mass selective detection, the utilization of D_2O allows for the isolation of hydroxyl stretching bands within $OH(D_2O)_n$ clusters. Two bands separated by 3 cm^{-1} are observed in the 3380 cm^{-1} region, and these are assigned to two isomers of $OH(D_2O)_2$ on the basis of frequency shifts, PUC dependence, and polarization spectroscopy. The isomers are both cyclic and differ only in the orientation of the non-bonded D atoms relative to the plane of the oxygen atoms, either "up-down" or "up-up." Calculations predict these isomers to be nearly isoenergetic (0.48 kJ/mol) and separated from each other by an approximately 2 kJ/mol barrier.

Four or five weak bands are observed in the 3150–3300 cm^{-1} region, all of which disappear upon cooling the pyrolysis furnace to room temperature (i.e., upon quenching the production of OH). Although less definitive than for the smaller clusters, PUC pressure measurements suggest that these bands are due to $OH(D_2O)_n$ clusters with $n > 2$. *Ab initio* computations of $OH(D_2O)_3$ clusters predict several nearly

isoenergetic isomers, again differing only in the orientation of the non-bonded D atoms. Assuming the above assignments, frequency shifts of the OH stretch in $OH(D_2O)_n$ clusters follow an approximately linear trend with increasing n (slope = 95 cm^{-1}). An approximately linear trend is also predicted *ab initio*, although the slope is overestimated by a factor of 1.5. Spectroscopic analysis of $OH(D_2O)_n$ clusters reveals that removing a hydrogen atom from $(H_2O)_{n>2}$ clusters does not affect significantly the incremental shifts of hydrogen bonded OH stretch vibrations as n increases from 2 to 4.[81]

ACKNOWLEDGMENTS

G. E. D. acknowledges support from the National Science Foundation (No. CHE-1054742). G. A. P. acknowledges CONICET, FONCyT, and SeCyT-UNC for financial support.

[1]M. N. Chan, H. F. Zhang, A. H. Goldstein, and K. R. Wilson, J. Phys. Chem. C **118**, 28978 (2014).
[2]T. Nah, H. F. Zhang, D. R. Worton, C. R. Ruehl, B. B. Kirk, A. H. Goldstein, S. R. Leone, and K. R. Wilson, J. Phys. Chem. A **118**, 11555 (2014).
[3]K. L. King, G. Paterson, G. E. Rossi, M. Iljina, R. E. Westacott, M. L. Costen, and K. G. McKendrick, Phys. Chem. Chem. Phys. **15**, 12852 (2013).
[4]C. Waring, K. L. King, P. A. J. Bagot, M. L. Costen, and K. G. McKendrick, Phys. Chem. Chem. Phys. **13**, 8457 (2011).
[5]P. A. J. Bagot, C. Waring, M. L. Costen, and K. G. McKendrick, J. Phys. Chem. C **112**, 10868 (2008).
[6]M. Allan, P. A. J. Bagot, M. L. Costen, and K. G. McKendrick, J. Phys. Chem. C **111**, 14833 (2007).
[7]K. S. Kim, H. S. Kim, J. H. Jang, H. S. Kim, B. J. Mhin, Y. M. Xie, and H. F. Schaefer, J. Chem. Phys. **94**, 2057 (1991).
[8]Y. M. Xie and H. F. Schaefer, J. Chem. Phys. **98**, 8829 (1993).
[9]B. S. Wang, H. Hou, and Y. S. Gu, Chem. Phys. Lett. **303**, 96 (1999).
[10]V. S. Langford, A. J. McKinley, and T. I. Quickenden, J. Am. Chem. Soc. **122**, 12859 (2000).
[11]S. Hamad, S. Lago, and J. A. Mejias, J. Phys. Chem. A **106**, 9104 (2002).
[12]Z. Y. Zhou, Y. H. Qu, A. P. Fu, B. N. Du, F. X. He, and H. W. Gao, Int. J. Quantum Chem. **89**, 550 (2002).
[13]A. Engdahl, G. Karlstrom, and B. Nelander, J. Chem. Phys. **118**, 7797 (2003).
[14]P. D. Cooper, H. G. Kjaergaard, V. S. Langford, A. J. McKinley, T. I. Quickenden, and D. P. Schofield, J. Am. Chem. Soc. **125**, 6048 (2003).
[15]P. C. do Couto, R. C. Guedes, B. J. C. Cabral, and J. A. M. Simoes, J. Chem. Phys. **119**, 7344 (2003).
[16]Y. Ohshima, K. Sato, Y. Sumiyoshi, and Y. Endo, J. Am. Chem. Soc. **127**, 1108 (2005).
[17]S. Y. Du, J. S. Francisco, G. K. Schenter, T. D. Iordanov, B. C. Garrett, M. Dupuis, and J. Li, J. Chem. Phys. **124**, 224318 (2006).
[18]S. Du, J. S. Francisco, G. K. Schenter, and B. C. Garrett, J. Chem. Phys. **128**, 084307 (2008).
[19]M. A. Allodi, M. E. Dunn, J. Livada, K. N. Kirschner, and G. C. Shields, J. Phys. Chem. A **110**, 13283 (2006).
[20]J. Gonzalez, M. Caballero, A. Aguilar-Mogas, M. Torrent-Sucarrat, R. Crehuet, A. Sole, X. Gimenez, S. Olivella, J. M. Bofill, and J. M. Anglada, Theor. Chem. Acc. **128**, 579 (2011).
[21]C. S. Brauer, G. Sedo, E. Dahlke, S. Wu, E. M. Grumstrup, K. R. Leopold, M. D. Marshall, H. O. Leung, and D. G. Truhlar, J. Chem. Phys. **129**, 104304 (2008).
[22]K. Tsuji and K. Shibuya, J. Phys. Chem. A **113**, 9945 (2009).
[23]P. Soloveichik, B. A. O'Donnell, M. I. Lester, J. S. Francisco, and A. B. McCoy, J. Phys. Chem. A **114**, 1529 (2010).
[24]S. Mitroka, S. Zimmeck, D. Troya, and J. M. Tanko, J. Am. Chem. Soc. **132**, 2907 (2010).
[25]E. Codorniu-Hernandez and P. G. Kusalik, J. Chem. Theory Comput. **7**, 3725 (2011).
[26]E. Codorniu-Hernandez and P. G. Kusalik, J. Am. Chem. Soc. **134**, 532 (2012).
[27]E. Codorniu-Hernandez and P. G. Kusalik, Phys. Chem. Chem. Phys. **14**, 11639 (2012).
[28]N. H. Do and P. D. Cooper, J. Phys. Chem. A **117**, 153 (2013).
[29]R. P. Wayne, *Chemistry of Atmospheres: An Introduction to the Chemistry of the Atmospheres of Earth, the Planets, and their Satellites*, 3rd ed. (Oxford University Press, Oxford, England, 2000).
[30]P. S. Monks, Chem. Soc. Rev. **34**, 376 (2005).
[31]J. H. Seinfeld and S. N. Pandis, *Atmospheric Chemistry and Physics: From Air Pollution to Climate Change* (Wiley, New York, 1998).
[32]R. Atkinson and J. Arey, Chem. Rev. **103**, 4605 (2003).
[33]K. Pfeilsticker, A. Lotter, C. Peters, and H. Bosch, Science **300**, 2078 (2003).
[34]R. J. Buszek, J. S. Francisco, and J. M. Anglada, Int. Rev. Phys. Chem. **30**, 335 (2011).
[35]S. Aloisio and J. S. Francisco, Acc. Chem. Res. **33**, 825 (2000).
[36]V. Vaida, J. Chem. Phys. **135**, 020901 (2011).
[37]B. Long, W.-J. Zhang, X.-F. Tan, Z.-W. Long, Y.-B. Wang, and D.-S. Ren, J. Phys. Chem. A **115**, 1350 (2011).
[38]J. Gonzalez, J. M. Anglada, R. J. Buszek, and J. S. Francisco, J. Am. Chem. Soc. **133**, 3345 (2011).
[39]R. J. Buszek, M. Torrent-Sucarrat, J. M. Anglada, and J. S. Francisco, J. Phys. Chem. A **116**, 5821 (2012).
[40]R. J. Buszek, J. R. Barker, and J. S. Francisco, J. Phys. Chem. A **116**, 4712 (2012).
[41]T. Zhang, W. Wang, C. Li, Y. Du, and J. Lu, RSC Adv. **3**, 7381 (2013).
[42]N. Karakus and R. Ozkan, J. Mol. Struct.: THEOCHEM **724**, 39 (2005).
[43]E. Vöhringer-Martinez, B. Hansmann, H. Hernandez, J. S. Francisco, J. Troe, and B. Abel, Science **315**, 497 (2007).
[44]C. Iuga, J. R. Alvarez-Idaboy, L. Reyes, and A. Vivier-Bunge, J. Chem. Phys. Lett. **1**, 3112 (2010).
[45]D. L. Thomsen, T. Kurten, S. Jorgensen, T. J. Wallington, S. B. Baggesen, C. Aalling, and H. G. Kjaergaard, Phys. Chem. Chem. Phys. **14**, 12992 (2012).
[46]C. S. Brauer, G. Sedo, E. M. Grumstrup, K. R. Leopold, M. D. Marshall, and H. O. Leung, Chem. Phys. Lett. **401**, 420 (2005).
[47]S. Wu, G. Sedo, and K. R. Leopold, J. Mol. Spectrosc. **253**, 35 (2009).
[48]A. Pabis, J. Szala-Bilnik, and D. Swiatla-Wojcik, Phys. Chem. Chem. Phys. **13**, 9458 (2011).
[49]J. P. Toennies and A. F. Vilesov, Angew. Chem., Int. Ed. **43**, 2622 (2004).
[50]M. Y. Choi, G. E. Douberly, T. M. Falconer, W. K. Lewis, C. M. Lindsay, J. M. Merritt, P. L. Stiles, and R. E. Miller, Int. Rev. Phys. Chem. **25**, 15 (2006).
[51]F. Stienkemeier and K. K. Lehmann, J. Phys. B: At., Mol. Opt. Phys. **39**, R127 (2006).
[52]K. Nauta and R. E. Miller, Science **287**, 293 (2000).
[53]G. E. Douberly and R. E. Miller, J. Chem. Phys. **122**, 024306 (2005).
[54]M. Hartmann, R. E. Miller, J. P. Toennies, and A. Vilesov, Phys. Rev. Lett. **75**, 1566 (1995).
[55]P. L. Raston, T. Liang, and G. E. Douberly, J. Chem. Phys. **137**, 184302 (2012).
[56]P. L. Raston, T. Liang, and G. E. Douberly, J. Phys. Chem. A **117**, 8103 (2013).
[57]K. Nauta and R. E. Miller, J. Chem. Phys. **115**, 10138 (2001).
[58]A. W. Hauser, A. Volk, P. Thaler, and W. E. Ernst, Phys. Chem. Chem. Phys. **17**, 10805 (2015).
[59]A. M. Morrison, T. Liang, and G. E. Douberly, Rev. Sci. Instrum. **84**, 013102 (2013).
[60]F. Dong and R. E. Miller, Science **298**, 1227 (2002).
[61]A. M. Morrison, S. D. Flynn, T. Liang, and G. E. Douberly, J. Phys. Chem. A **114**, 8090 (2010).
[62]T. Liang, D. B. Magers, P. L. Raston, W. D. Allen, and G. E. Douberly, J. Chem. Phys. Lett. **4**, 3584 (2013).
[63]M. J. Frisch, G. W. Trucks, H. B. Schlegel, G. E. Scuseria, M. A. Robb, J. R. Cheeseman, G. Scalmani, V. Barone, B. Mennucci, G. A. Petersson, H. Nakatsuji, M. Caricato, X. Li, H. P. Hratchian, A. F. Izmaylov, J. Bloino, G. Zheng, J. L. Sonnenberg, M. Hada, M. Ehara, K. Toyota, R. Fukuda, J. Hasegawa, M. Ishida, T. Nakajima, Y. Honda, O. Kitao, H. Nakai, T. Vreven, J. A. Montgomery, Jr., J. E. Peralta, F. Ogliaro, M. Bearpark, J. J. Heyd, E. Brothers, K. N. Kudin, V. N. Staroverov, R. Kobayashi, J. Normand, K. Raghavachari, A. Rendell, J. C. Burant, S. S. Iyengar, J. Tomasi, M. Cossi, N. Rega, N. J. Millam, M. Klene, J. E. Knox, J. B. Cross, V. Bakken, C. Adamo, J. Jaramillo, R. Gomperts, R. E. Stratmann, O. Yazyev, A. J. Austin, R. Cammi, C. Pomelli, J. W. Ochterski, R. L. Martin, K. Morokuma, V. G. Zakrzewski, G. A. Voth, P. Salvador, J. J. Dannenberg, S. Dapprich, A. D. Daniels, Ö. Farkas, J. B. Foresman, J. V. Ortiz, J. Cioslowski, and D. J. Fox, GAUSSIAN 09, Revision D.01, Gaussian, Inc., Wallingford, CT, 2009.
[64]A. Scheidemann, B. Schilling, and J. P. Toennies, J. Phys. Chem. **97**, 2128 (1993).
[65]J. Q. Searcy and J. B. Fenn, J. Chem. Phys. **61**, 5282 (1974).
[66]L. Belau, K. R. Wilson, S. R. Leone, and M. Ahmed, J. Phys. Chem. A **111**, 10075 (2007).

[67]F. J. Hernandez, J. T. Brice, C. M. Leavitt, G. A. Pino, and G. E. Douberly, J. Phys. Chem. A **119**, 8125 (2015).
[68]E. P. Hunter and S. G. Lias, "Proton affinity evaluation," in *NIST Chemistry WebBook*, NIST Standard Reference Database Number Vol. 69, edited by P. J. Linstrom and W. G. Mallard (National Institute of Standards and Technology, Gaithersburg, MD, 2015), http://webbook.nist.gov.
[69]M. Lewerenz, B. Schilling, and J. P. Toennies, J. Chem. Phys. **102**, 8191 (1995).
[70]D. P. Schofield and H. G. Kjaergaard, J. Chem. Phys. **120**, 6930 (2004).
[71]M. D. Marshall and M. I. Lester, J. Chem. Phys. **121**, 3019 (2004).
[72]M. D. Marshall and M. I. Lester, J. Phys. Chem. B **109**, 8400 (2005).
[73]G. E. Douberly, P. L. Raston, T. Liang, and M. D. Marshall, J. Chem. Phys. **142**, 134306 (2015).
[74]C. P. Moradi and G. E. Douberly, J. Mol. Spectrosc. **314**, 54 (2015).
[75]G. E. Douberly and R. E. Miller, J. Phys. Chem. B **107**, 4500 (2003).
[76]K. J. Franks, H. Z. Li, and W. Kong, J. Chem. Phys. **110**, 11779 (1999).
[77]W. Kong and J. Bulthuis, J. Phys. Chem. A **104**, 1055 (2000).
[78]W. Kong, L. S. Pei, and J. Zhang, Int. Rev. Phys. Chem. **28**, 33 (2009).
[79]N. Pugliano and R. J. Saykally, Science **257**, 1937 (1992).
[80]J. C. Owicki, L. L. Shipman, and H. A. Scheraga, J. Phys. Chem. **79**, 1794 (1975).
[81]C. J. Burnham, S. S. Xantheas, M. A. Miller, B. E. Applegate, and R. E. Miller, J. Chem. Phys. **117**, 1109 (2002).